Towards a compact XYZθ positioning system with built-in actuators using 3^D printing of conductive polymer

Benjamin Calmé, Lennart Rubbert, Yassine Haddab

To cite this version:

Benjamin Calmé, Lennart Rubbert, Yassine Haddab. Towards a compact XYZθ positioning system with built-in actuators using 3^D printing of conductive polymer. Journal of Micro-Bio Robotics, 2023, 18, pp.61-74. 10.1007/s12213-023-00159-4 . hal-04157389

HAL Id: hal-04157389
https://hal.science/hal-04157389v1

Submitted on 10 Jul 2023

Towards a compact XYZθ positioning system with built-in actuators using 3D printing of conductive polymer

Benjamin Calmé[1,2*], Lennart Rubbert[2†] and Yassine Haddab[1†]

[1*]LIRMM, University of Montpellier, CNRS, 161 rue Ada, Montpellier, 34095, France.
[2]ICube, University of Strasbourg, CNRS, 24 Bld de la Victoire, Strasbourg, 67084, France.

*Corresponding author(s). E-mail(s): benjamin.calme@lirmm.fr;
Contributing authors: lennart.rubbert@insa-strasbourg.fr; yassine.haddab@umontpellier.fr;
†These authors contributed equally to this work.

Abstract

Technological advances in additive manufacturing have made it possible to exploit composite materials, such as carbon-doped filaments, synthesised for specific function with tailored properties. The integration of carbon fibres, with good electrical and thermal conductivity, within an insulating polylactic acid (PLA) matrix produces a conductive functional material. These properties allow to manufacture mesoscopic electrothermal actuators and more complex monolithic structures including them. A compact and monolithic 3D printable positioning system with built-in V-shaped actuators is proposed in this paper. The prototype presented has an 86.2mm$^{\mathbf{3}}$ workspace for a particularly compact footprint, i.e. 206mm×109mm×21mm. In this system, the linear motions along the X and Y axes are decoupled from the linear motion along Z, which is also decoupled from the rotation θ around Z, thus simplifying future kinematic control strategies. Multi-physics coupling analyses are performed in ANSYS to validate the estimated performance of each component of the positioning system. Then, experimental characterisations based on 3D printed prototypes were carried out and showed good agreement between models and experiments. These first results also include the implementation of a first closed loop control strategy using a Smith predictor.

Keywords: Mechanism design, Electrothermal actuators, Compliant Mechanism, Mechanism analysis, Additive manufacturing

1 Introduction

Miniaturisation proved to be of great importance in several areas of mechatronics, such as medical robotics or space applications. Technological advances in these fields have made it possible to produce smaller, more compact and therefore more portable devices [1, 2]. However, this down scaling is more complex for traditional actuators and is associated with a difficult assembly phase. The miniaturisation of traditional devices such as electric motors, pneumatic and hydraulic actuators comes at the cost of a significant decrease in performance. Hence, in mesorobotics and microbotics, actuators of different natures tend to replace traditional actuation technologies [3]. These include thermomechanical actuators [4], some of which can be regarded as flexible mechanisms. U-shaped [3], V-shaped and Z-shaped actuators [5] are the three main electrothermal flexible actuators able to produce planar displacements. This is a clear advantage when designing compliant structures with built-in actuators[6, 7]. In addition to being scalable and monolithic, flexible mechanisms have many advantages in terms of accuracy and repeatability due to the avoidance of wear and mechanical play because of the absence of contact and therefore friction.

The technological development of manufacturing methods, such as additive manufacturing, and the research for new types of materials have led to more freedom in design. Composite materials, such as carbon-doped PLA, obtained by infusing carbon fibres into a polymer matrix, have resulted in a functional material with improved mechanical behaviour and new physical properties [8]. Carbon fibres are particularly known in engineering for their good mechanical characteristics due to their crystalline structure. They also have good conductive properties due to the sp^2 hybridisation of the carbon atoms. The initially insulating polymer becomes, for a minimal inclusion of carbon fibres, a conductive composite material. The design of actuators based on doped material, e.g. carbon doped resin, using Joule effect and thermal expansion have already been investigated [7, 9]. However, the manufacturing process used in this study is demanding as it requires resin preparation and access to a dedicated additive manufacturing process. In contrast, carbon-doped PLA, which is compatible with standard 3D printers, is an available material and has been investigated for its conductivity for sensor development [10, 11], but has not, to the authors' knowledge, been exploited for actuator design.

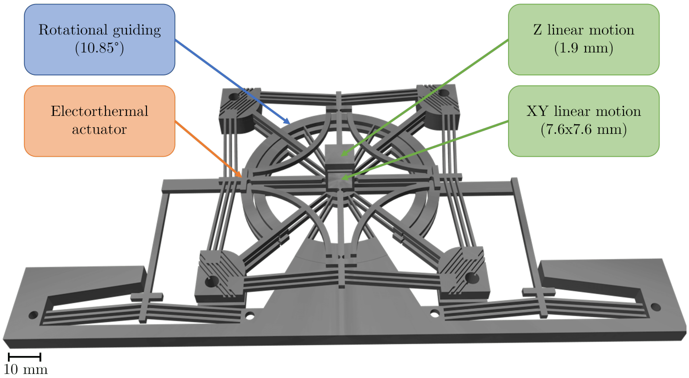

Fig. 1 Structure of the 3D-printed monolithic XYZθ positioning system. The maximum strokes achieved in the experiment are shown for each axis.

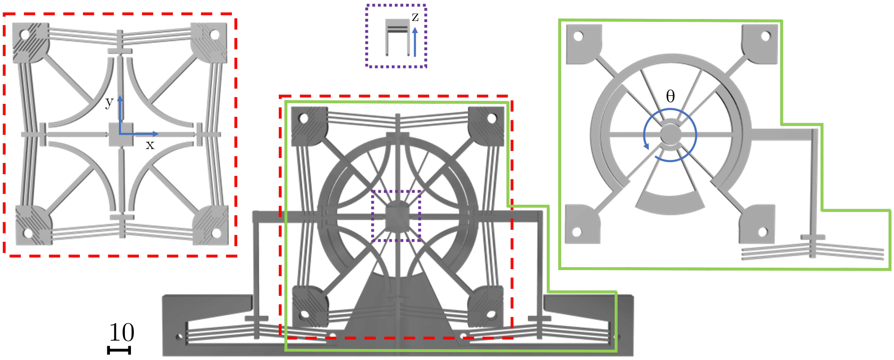

Fig. 2 Structure of the 3D-printed monolithic XYZθ positioning system (unit: mm). The movements allowed per component are indicated by the arrows.

While only conductive aspects have been explored for carbon-doped PLA as well as sensor applications [10–13], the potential of 3D printed actuators is too large to be disregarded. The contributions of this paper include demonstrating the feasibility of 3D printing mesoscopic actuators through modelling and experimental validation, and proposing an approach to include them within the structure, which has potential for robotic applications [6]. In order to demonstrate the viability of the approach, a proof of concept has been realized consisting of a compact (90cm^3) 3D printable positioning system with integrated actuators, as shown in Fig. 1. The originality of the design proposed in this paper lies in the use of the freedom offered by 3D printing to be able to monolithically manufacture the positioning system, the six independent actuators and the cooling system. The system is therefore ready to use, inexpensive and can be manufactured with the majority of PLA-compatible 3D printers, as shown in Fig. 3. The first elements of a readily usable closed-loop control strategy are also provided.

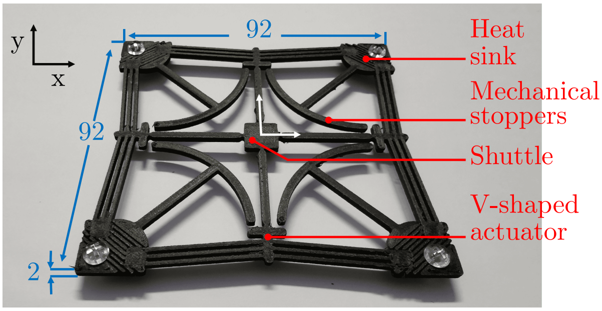

Fig. 3 3D-printed monolithic compliant mechanism for XY linear guiding (unit: mm).

The paper is organised as follows. In Section II, the design of the positioning system and the analytical model of its components are introduced. The design and modelling of the electrothermal actuator are presented in Section III. In Section IV, The results of the finite element analyses and their correspondence with the results obtained from the experimental characterisation are detailed. The preliminary results of the control strategy are given in Section V and the conclusions are provided in Section VI.

2 Design and analysis of the XYZθ positioning system

The positioning system is based on an arrangement of several components that allow different motions in the workspace. Fig. 2 shows a top view of the platform with the identification of the three major components, namely the system allowing linear displacement along the X and Y axes, in a dashed line, the system allowing the rotation around the Z-axis, outlined in a solid line, and the linear displacement along Z in profile view and framed by a dotted line. The rotational guiding component is present twice in a symmetrical manner in order to be able to carry out clockwise and counter-clockwise rotations. These components are manufactured to have a decoupled operation and will be successively characterised in this section.

2.1 Compliant mechanism for X and Y linear motions

2.1.1 Operational principle

The first component of the platform studied is the compliant mechanism allowing a two-axis linear movement, as illustrated in Fig. 3. This mechanism consists of a central shuttle and four actuators in opposition two by two. Each actuator is connected to the platform by means of a beam and a flexible joint, i.e. circular hinges. The choice of a circular hinges rather than the more kinematically efficient crossbar pivot joint is related to the 3D printing manufacturing process. A circular hinge is easier to print because of its flat geometry and are less cumbersome. These passive links allow the platform to

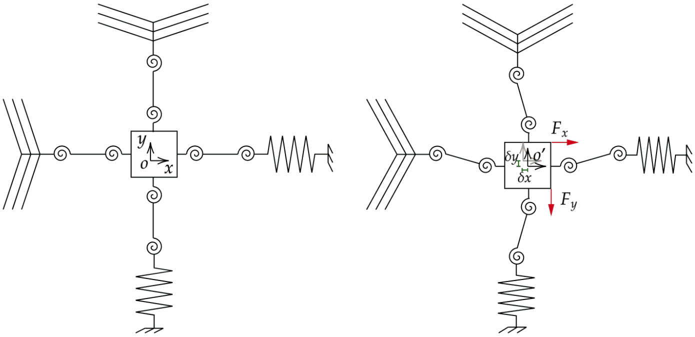

Fig. 4 Illustration of the working principle of the compliant mechanism for linear motions on two axes. Deflections and compressions are represented by spiral and linear springs.

move in the workspace in response to the actuators, as shown in Fig. 4. When a force F is produced by one or two actuators, the platform changes its position according to single or dual axis components, $O' = (\delta_x, \delta_y)^T$. The figure shows the operating principle of the XY guide mechanism and the effect of the actuation of the left and top actuators. The linear springs represent the compression of the actuators in opposition. The spiral springs symbolise the mobility of the bars around the circular hinges allowing the movement.

2.1.2 Actuation against opposite actuators

The actuators are in opposition two by two. When one is actuated, the other is loaded and must deform. It is therefore necessary to calculate the force-displacement relationship of the actuator at rest when it is loaded. This quantity allows to know the minimum force F that the active actuator must provide to deform the one at rest depending on the geometrical parameters of the actuator, i.e. α the angle of inclination of the beams and L the length of the beams. The V-actuator is shown in Fig. 3 and is described in detail in section 3. The force-displacement characteristic curve of this pre-shaped mechanism has two domains. A linear domain in which the evolution of the force f, is calculated as follows [14]:

$$f = 8\pi^2 \frac{EI\sin\alpha}{(L)^2}\left(\frac{4}{3} - \frac{y}{L\sin\alpha}\right) \tag{1}$$

And a non-linear domain where the relationship between the force f, the normalized axial force N and the deformation generated by the active actuator y is calculated according to [14], as follows:

$$f = \frac{EI\sin\alpha}{8(L)^2}\left(\frac{N^3}{\frac{N}{4} - \tan\frac{N}{4}}\right)\left(\frac{N^2}{N^2 - 4\pi^2} - \frac{y}{L\sin\alpha}\right) \tag{2}$$

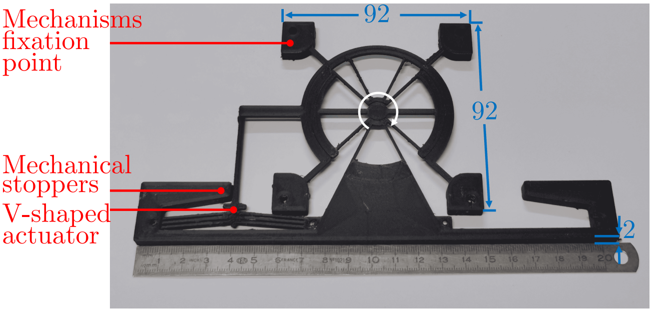

Fig. 5 3D-printed monolithic compliant mechanism for θ rotational guiding (unit: mm).

$$\begin{aligned}\frac{3}{16N^4}\left(1+\frac{\tan^2(N/4)}{3}-\frac{\tan(N/4)}{(N/4)}\right)f^2-\frac{4\pi^2}{(N^2-4\pi^2)^2}f\\+\frac{N^2}{12(L\sin\alpha/w_b)^2}-\frac{N^2\pi^2(N^2-8\pi^2)}{4(N^2-4\pi^2)^2}=0\end{aligned} \tag{3}$$

where I is the quadratic moment of the beam and $N = \sqrt{\mu(2L)^2/(EI)}$ with μ the axial force. The solution is given by a numerical method.

2.2 Compliant mechanism for rotational guiding

The achievement of a pure and large rotational motion with flexible mechanisms is often a little less trivial. Among the solutions presented in the literature, the flexible butterfly pivot was chosen. This choice was made due to the amplitude of movement allowed by this type of joint, the optimisation of which can lead to angles close to $\theta = \pi/2$, and the small parasitic shift of the centre of rotation.

This joint was described by Henein et al. [15, 16] as a series connection of four RCC (Remote Center of Compliance) pivots with two beams, shown in Fig. 5. The four pivots have the particularity of having the same centre of rotation. The performance described above is due to this high degree of symmetry.

2.2.1 Angular stiffness and admissible angular stroke

The calculation of the angular stiffness of an RCC connection is defined by the ratio between the moment applied to the joint M and the resulting angular motion θ. According to [17], it can then be calculated according to the following equation:

$$K_\theta = \frac{M}{\theta} = \frac{8EI}{l}\left(1+\frac{3p}{l}+\frac{3p^2}{l^2}\right) \tag{4}$$

With p and l the geometrical distance parameters shown in Fig. 6. The applied moment generates mechanical stresses in the beams with a maximum value at the central anchoring point. From [17], it is then possible to derive a maximum

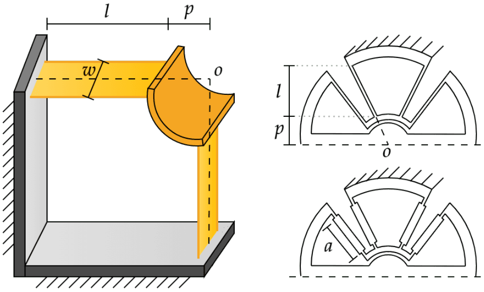

Fig. 6 Scheme of a two-blade RCC pivot and its integration into a half-pin (symmetrical on both sides of the axis)

admissible angle stroke based on an admissible stress, σ_{adm}:

$$\theta_{adm} = \frac{\sigma_{adm} l^2}{Ew(2l + 3p)} \tag{5}$$

with w the thickness of the beam. A version with a reinforced structure against out of plane motion, inspired by previous work [18], was also investigated. This variant is considered because of the stacking of the structures which should increase transverse stiffness. Based on the new design calculations, a new value for the stiffness $K_{\theta|R}$ and angular deflection $\theta_{adm|R}$ is found:

$$K_{\theta|R} = EI \frac{a^2 + al + 4(l^2 + 3lw + 3w^2)}{(l - a)(a^2 + al + l^2)} \tag{6}$$

$$\theta_{adm|R} = \frac{4\sigma_{adm}}{Ew} \frac{(l - a)(a^2 + al + l^2)}{a^2 + al + 2l(2l + 3w} \tag{7}$$

with a the length of the reinforcing element, as shown in Fig. 6.

2.2.2 Actuation of the Butterfly joint

When sizing the actuator, two aspects must be taken into account. The force to be produced and the displacement. In order to limit the size of the structure, the constraint was set to use an actuator identical to those used for the linear guide. This constraint allows a dimensioning with equivalent stiffness. In other words, the sizing is done in such a way that the stiffness of the butterfly link is equal to that of a V-shaped actuator at rest [19], which means that the equations are solved according to whether the joint is reinforced or not:

$$K_{\theta} = K_{\theta|R} = K_a = \frac{2nE(12I\cos^2\theta + A_b L^2 \sin^2\theta)}{L^3} \tag{8}$$

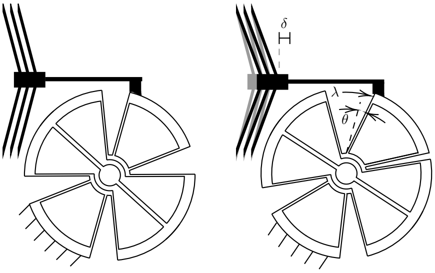

Fig. 7 Schematic of a two-blade RCC pivot and its integration into a half-pin (symmetrical on both sides of the axis)

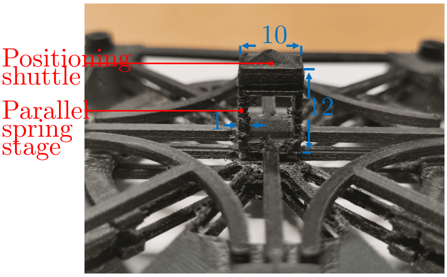

Fig. 8 3D-printed monolithic Z linear guiding (unit: mm).

Assuming that the arc λ produce by the force F can be approximated by a linear motion, $\lambda = \Delta x$, it is then possible to express the achievable θ_{max} as

$$\theta_{max} = \operatorname{atan}\left(\frac{\lambda}{l+p+d}\right) \simeq \frac{\lambda}{l+p+d} \tag{9}$$

where d is the distance between l and the anchor on the actuator as shown in Fig. 7. In order to allow control of the rotation in both directions, the choice was made to stack two butterfly joints on top of each other, with an offset by an angle $\beta = \pi/2$. Each of these joints was operated by an independent actuator.

2.3 Implementation of a motion along Z

The addition of the Z-translation was achieved by adding a variant of a thin parallel spring stage, as shown in Fig. 8. This mechanism was designed to rely solely on the principle of thermal expansion due to the passage of an electric current. On the same principle as the thermal actuator used, following the application of a current, thermal expansion due to the Joule effect will allow the central shuttle to move along the Z-axis.

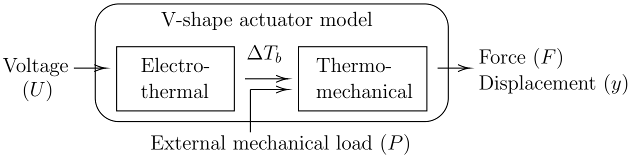

Fig. 9 Schematic representation of the analytical modelling of the actuator

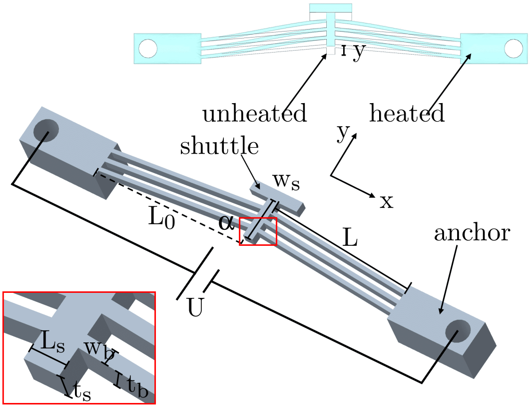

Fig. 10 CAD model illustration of the V-shaped electrothermal actuator and parameter identification.

3 Design and modelling of the electrothermal actuator

In order to build a 2D positioning system, V-shaped actuators are used. In fact, Z-shaped actuators showed poorer performance in terms of output force and motion magnitude [5], and since rectilinear motion is expected, U-shaped actuators are excluded. The V-shaped actuator consists of two beams, inclined at an angle α, fixed to a central shuttle on one end and anchored on the other.

3.1 Analytical model of the V-shape actuator

The design and functioning of this actuator are based on the use of carbon fibres within the PLA. When a voltage is applied to the actuator, the natural electrical resistance induces Joule heating. The temperature generated leads to thermal expansion, symmetrically varying the length of the beams and thus causing the displacement of the central shuttle y. Consequently, the analytical modelling of this type of actuator is done in two steps, a first step to model the electrothermal effect and a second step to model the thermomechanical effect, as shown in Fig. 9.

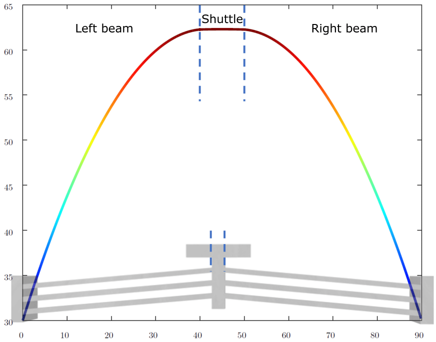

Fig. 11 Temperature distribution within the actuator based on the analytical model.

3.1.1 Electrothermal Model

when a voltage is applied, the heat generated by the Joule effect is dissipated simultaneously by radiation and convection until a steady state thermal equilibrium is reached. Both of this thermal mechanisms can be neglected at first with small scale actuator. According to [20], the average temperature increase along the beams ΔT_b is defined as function of the input voltage U, geometrical parameters of the beam Π and the material properties Q as follows:

$$\Delta T_b = \frac{1}{L}\int_0^L (T_s - T_0) = Q\Pi U^2 \tag{10}$$

with,

$$Q = \frac{1}{k_a \rho}, \quad \Pi = \frac{\left(1 - e^{L\Gamma}\right)^2}{Le^{L\Gamma}\Gamma}\varphi + \left(\frac{1 - e^{L\Gamma}}{Le^{L\Gamma}\Gamma} + 1\right)\chi \tag{11}$$

where $\Gamma = \sqrt{k_a/(kt_b)}$, L is the beam length, k_a is the thermal conductivity of the air, k is the thermal conductivity of beam, ρ is the electric resistivity. The calculation details of φ and χ, which are depending on the geometrical parameters, shown in Fig. 10, are clearly presented in [20].

In Fig. 11, the temperature distributions along the actuator, analytically calculated, is given for $U = 50V$. The shuttle has the highest temperature due to its greater resistivity. The temperature of 60 degrees is the limit for PLA before glass transition. Exceeding this glass transition temperature will result in a change in the behaviour of the material, which will tend to a plastic deformation.

3.1.2 Thermomechanical Model

According to [20], considering the symmetry of the actuator and the shuttle as infinitely rigid and not subject to thermal expansion, then the shuttle displacement is obtained from the following Castigliano theorem:

$$y = \Delta L_T \sin\alpha - \int_0^L \frac{N}{EA_b}\frac{\partial N}{\partial P}dx - \int_0^L \frac{M}{EA_b}\frac{\partial M}{\partial P}dx \tag{12}$$

where ΔL_T is the axial elongation of the beam linked to thermal expansion, α is the inclination angle of the beam and A_b the beam cross section area. M and N are the bending moment and the axial force on the beam. E is the Young's modulus of the beam material. This equation can be simplified by substituting boundary conditions, such as

$$y = \begin{pmatrix} \alpha L\Phi \sin\alpha & -L\frac{\Phi}{EA_b} \end{pmatrix} \begin{pmatrix} \Delta T_b \\ P \end{pmatrix}, \tag{13}$$

where α is the coefficient of thermal expansion and $\Phi = L_0^2/(h_0^2\cos^4\theta + L_0^2\sin^2\theta)$. L_0 is the distance between the two anchor points of the beam. The elements of the left-hand side of Eq. (13) thus represent the flexibility of the actuator in response to the temperature and in response to an external load P. The load P will be the spring force of the actuator mounted in opposition in the case of the positioning system, as shown in Fig. 12.

3.1.3 Combined actuator models

By combining the two models, Eq. (13) can be rewritten as follows :

$$y = \begin{pmatrix} \alpha L_0\Gamma \sin\theta QT & -\frac{L_0\Gamma}{EA_b\cos\theta} \end{pmatrix} \begin{pmatrix} U^2 \\ P \end{pmatrix} \tag{14}$$

$$= (\kappa_1 - \kappa_2) \begin{pmatrix} U^2 \\ P \end{pmatrix} \tag{15}$$

By modelling the force related to an input voltage as a spring pushing the shuttle, the equation for the force F produced by the actuator can be established as follows [20]:

$$F = \xi U^2 - P \quad \text{with} \quad \xi = \frac{\kappa_1}{\kappa_2} \tag{16}$$

3.2 Voltage distribution in the monolithic XY compliant mechanism

In order to produce the 2D positioning system, the insulation of the part between the different actuators must be done. The first approach is only relevant for certain category of 3D printers, able to extrude different materials during the same printing process. This option offers the opportunity to print the entire platform as a single rigid piece by connecting the actuators, printed in carbon PLA, with an electrically insulating polymer, as shown in Fig. 13a.

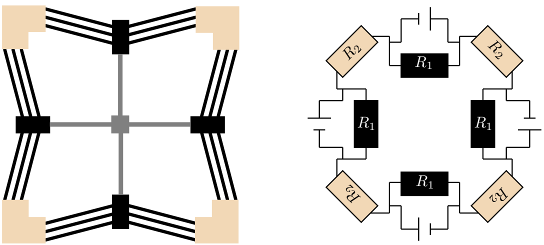

Fig. 12 Electrical representation based on a resistor set equivalent to the monolithic positioning system.

The main contribution is done for single extruder printers, in order to make it compatible with the largest number of printers, the phenomena of electrical and thermal conduction in the design have to be considered, as shown in Fig. 13d. The first step is to model the mechanism as a series of resistors. A perfect electrical insulator has infinite resistance, which can be expressed in the design, according to Fig. 12, as $R_2 \gg R_1$. In order to increase the resistance R, the length l and resistivity ρ have to be maximised and the cross-section s has to be minimised, according to the following equation:

$$R = \rho \frac{l}{s} \tag{17}$$

The first aspect to consider is that although the material has become conductive due to the carbon, it retains a high electrical resistivity. Then, the conductive properties of the printed material are dependent of the orientation of the neutral fibres, which is defined by the direction of movement of the nozzle. According to [13], a 100% infill pattern with lines was then chosen to maximise the electrical resistivity.

During the design process, the application of a simple pattern allowed the cross-section to be reduced by exploiting the smallest printing parameters allowed by the printer. The pattern to reduce the cross-sectional area was also chosen to exploit the laminar flow cooling properties of the heat sinks and thus avoid heat conduction to the adjacent actuators.

Hence, from the previously calculated maximum force of the actuator F_{max}, it is possible to define the maximum deformation and thus the maximum displacement of the positioning system platform. Knowing F_{max} and y_{max} of the actuator calculated in the electro-thermo-mechanical model, it is then possible to define the expected motion of the manipulator.

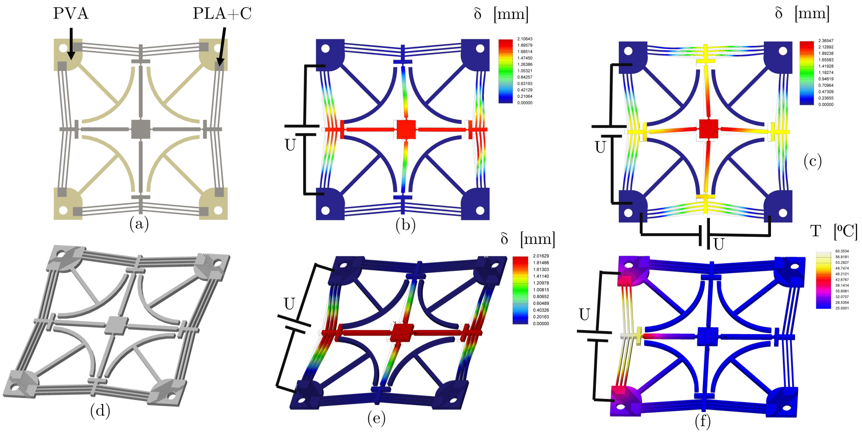

Fig. 13 Finite element simulation result for a 2D positioning system. (13a) represents the CAD of the positioning system manufactured in bi-material. (13b) and (13c) illustrate the simulation results obtained by FEA following the actuation of the left actuator and the left and bottom actuators. (13d) represents the CAD of the monolithic positioning system. (13e) and (13f) illustrate the thermomechanical and electrothermal FEA results of the same simulation, following the actuation of the left actuator with the monolithic positioning system. The sub-figures (13d)(13e)(13f) are illustrated in perspective in order to visualise the pattern used to increase the resistance of the sections between actuators.

4 Finite element analysis and experimental characterisation

4.1 Multiphysics Finite Element Analysis

The multiphysics numerical simulation was performed with the ANSYS solver implemented in Creo Parametric 6.0. The analyses were conducted by coupling the electrical, thermal and mechanical fields. The geometrical parameters used for the XY compliant mechanism are shown in Tab. 1. The properties of the material used in the simulations are derived from an experimental characterisation phase as explained in subsection 4.2.

The model is set to couple the multiphysics phenomena, while assuming constant materials properties. In other words, the electric current flowing through the actuator will heat the material, but the increase in temperature and deformation of the material will not affect the current. Non-linearities will be integrated in future optimisation study. For the thermoelectric simulation a voltage was applied to the conductive material and thus simulate heat generation by Joule effect. The faces of the actuator are set to a convective heat boundary condition, simulating the air temperature around with the heat flux option. The simulation results for the positioning system are shown in Fig. 13. Simulations have been carried out for a dual-material positioning system and for a single-material positioning system. Simulation results with one or two actuators operating simultaneously are presented Fig. 13b and Fig. 13c. The

Table 1 Design parameters

Material parameters						
E [MPa]	E' [MPa]	R [Ohm]	R' [Ohm]	ρ [Ohm.m]	d [$Kg.m^{-3}$]	k [$Wm^{-1}K^{-1}$]
3300	3140	800-1200	900	0.06	1150	0.366
Geometric parameters						
L [mm]	α	L_0 [mm]	$t_s = t_b$ [mm]	w_s [mm]	w_b [mm]	L_s [mm]
30	5	29.89	2	8	0.8	2

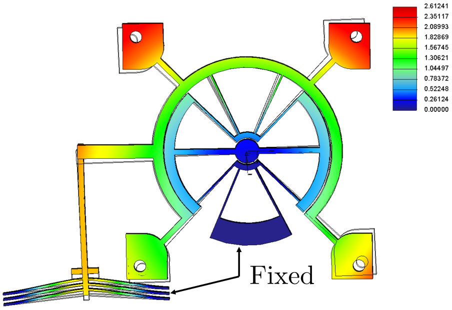

Fig. 14 Finite element simulation result of the rotational guiding system (displacement in mm).

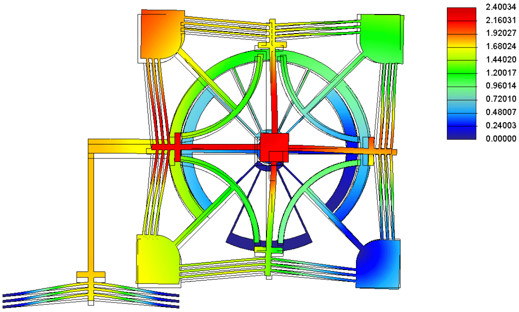

Fig. 15 Finite element simulation result of the monolithic XYZθ system (displacement in mm).

feasibility of the single-material mechanism is shown in Fig. 13e and Fig. 13f corresponding to the same simulation, illustrating mechanical and thermal analysis respectively.

The stroke of the mechanism is almost the same as for the mechanism with insulating material, which proves that the design does not affect the performance. The electro-thermal simulation shows that the temperature in the actuator, through which the current flows, does increase. It also shows that the temperature in the other actuators is not affected by the heating. The actuators can therefore be controlled independently.

The butterfly joint simulations validated the stiffness design model as the actuator achieves the same order of magnitude of displacement as previously with the linear guide for the same temperature, as shown in Fig. 14. This performance is slightly lower for the monolithic mechanism, as shown in Fig. 15. The result for a coupled actuation at a temperature of 40°C is a displacement of 2.03mm in X, 1.97mm in Y, 1.2mm in Z and a rotation of 3.8°. For a maximum temperature of 58°C, the maximum rotation is 5.85° for one butterfly joint and thus 11.7° for two. This movement can be coupled with displacements of 4.1mm along X and Y and 2mm along Z. According to these results, the platform moves in a simulated space of 105.6mm^3.

4.2 Experimental characterisation of the material

The material used for these experiments is Original Carbon Fiber PLA (Proto Pasta). It was printed with an Ultimaker S3 at an extrusion temperature of 240°C degrees, at a speed of 30mm/s on a bed heated to 60°C.

Resistance R' was measured with an ohmmeter. The sample to be measured was placed between the probes of the ohmmeter. The resistivity ρ was then calculated according to Eq. (17). Electrical heating performance of the sample was determined based on surface temperature with various applied voltages while using a DC power supply. The range of applied voltage was from 20V to 50V with 5V intervals. As the contact could not be made by soldering, it was made by means of a screw-nut embedding. A K-type thermocouple was used to measure the surface temperature after applying different voltages.
The mechanical characterisation of the material was carried out with a FK50 force sensor (Sauter) and a LK-H152 laser-based displacement sensor (Keyence), as detailed in [21]. A beam was printed with carbon-PLA and the Young's modulus E' was characterised using Euler Bernoulli's relationship between applied force F and measured displacement δ:

$$\mathrm{E}' = \frac{\mathrm{F}\mathrm{L}^3}{3\delta \mathrm{I}} \tag{18}$$

where I the quadratic moment of the cross section and L the length of the beam. The characterized Young's modulus is 3140MPa, which is consistent with some earlier characterisation of the material [22].

4.3 Experimental characterisation of the V-shaped electrothermal actuator

The behaviour of the actuator was characterised experimentally by means of the experimental set-up shown in Fig. 16. The shuttle displacement was measured for different voltage values ranging from 10 to 50V in 5V steps and with a return to room temperature in between. The experimental results are presented in Fig. 17. The experimentally measured values are in good accordance with the results of previous models.

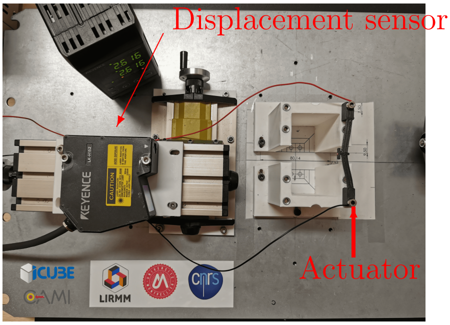

Fig. 16 Experimental set-up for the characterisation of the electro-thermal actuator.

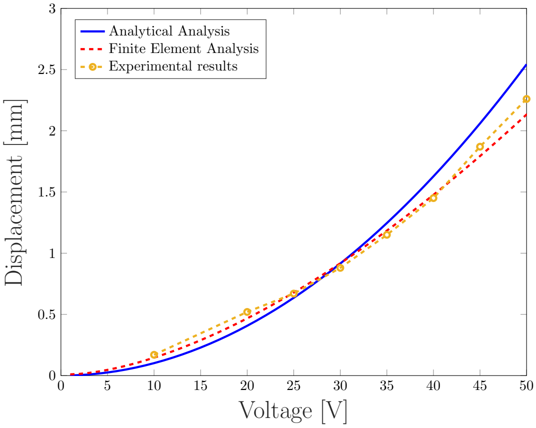

Fig. 17 Displacement obtained for the electrothermal actuator as a function of the input voltage.

At 55V, the temperature of the measured actuator was 64°C, i.e. beyond the glass transition phase indicated by the manufacturer. It is noted that after reaching this temperature, the actuator does not recover its initial configuration. The displacement sensor indicates a position of 0.13mm despite the mechanism returning to room temperature.

4.4 Experimental characterisation of the positioning system

The performance of the positioning system has been analysed using the same equipment as before, as shown in Fig. 18. After applying a voltage to one of the actuators, the displacement of the central shuttle was measured using the displacement sensor. By driving an actuator with a conservative voltage of 50V, an average motion range of 3.34mm is achieved, as shown in Fig. 19. This also corresponds to a total motion range of 6.68mm along each axis. For a given desired position, the manipulator was operated 21 times with a open

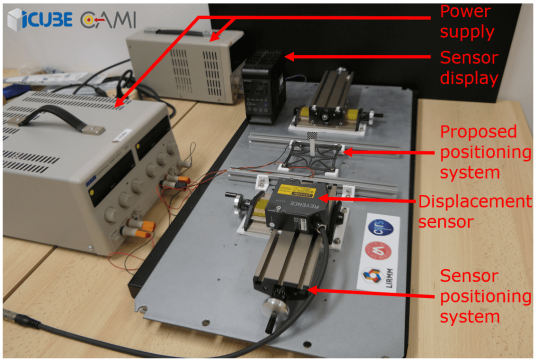

Fig. 18 Experimental setup of the XY positioning system.

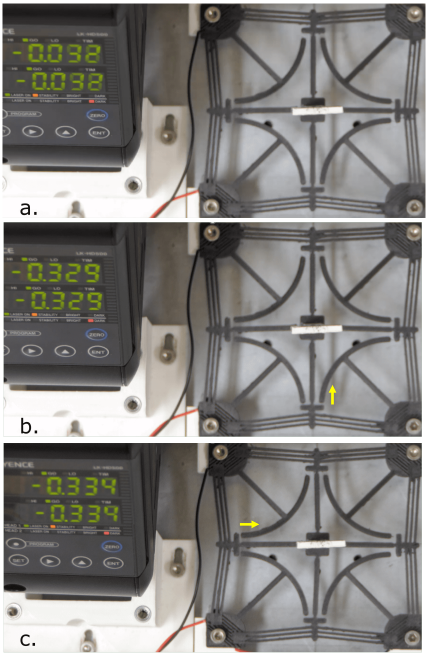

Fig. 19 Experimental setup of the XY positioning system. The numbers on the dials of the Keyence sensor show the displacement in centimetres. The top image (a.) represents the initial state and the middle (b.) and bottom (c.) images show the amount of displacement in the direction of the arrows in response to an actuation.

loop voltage of 40V. The average displacement measured was 2.17mm and the standard deviation was 0.19mm.

An error of 17% is found between the actuator estimated and measured values. However, an error of only 4% is found between the measured and estimated force-displacement relationship with respect to the opposite actuator. In line with the fact that these are preliminary results obtained with

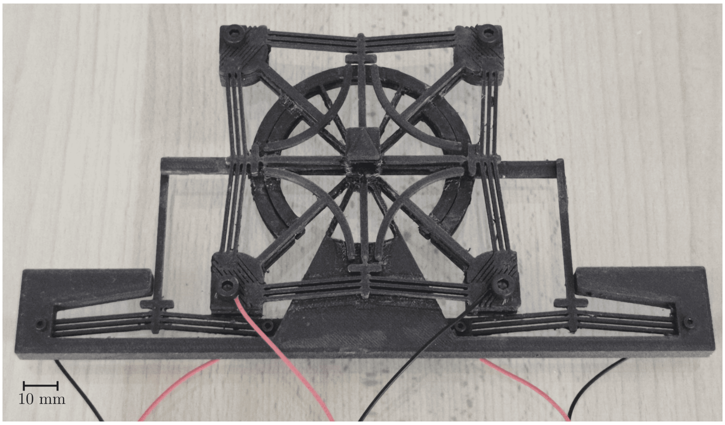

Fig. 20 3D printed monolitic XYZθ positioning system

Table 2 Performance comparisons between the proposed XY positioning system and previous reported parallel stages (*FEA results)

References	Actuator	Dimension [mm]	Motion range
[26]	piezoelectric	50×50×10	14×14 [µm]
[27]	electromagnetic	120×120×25	11×11,6 [mm]
[28]	*theoretic**	300×300×27	5×5 [mm]
[29]	*theoretic**	200×200×10	4×4 [mm]
Proposed [30]	electrothermic	92×92×2	3,7×3,7 [mm]

an open-loop control and with a 3D printed composite material, thus particularly non-linear, the error obtained shows that the order of magnitude of the model estimates is satisfying. As presented in Tab. 2 and in Tab. 3, given the millimetre range of motion achieved, the objective of designing a compact and low-cost positioning system is successfully achieved. The presence of nonlinear effect requires the implementation of control strategy in order to achieve a precision positioning. The precepts are introduced in the following section.

Carbon composite is still a fairly demanding material and requires a number of fine tunings of the printer to achieve a structure as complex as the one presented in Fig. 20. Furthermore, the characterisation of the material showed sufficient rigidity for use with conventional blades in the butterfly joint. This result was confirmed by obtaining the functional platform, shown in Fig. 20. This flexible rotary guidance, whose performance is shown in Fig. 21, could however be further improved by an optimisation phase [23, 24] and amplified [25]. The individual performance of the actuators within the platform allows linear displacements of up to 3.8 mm and a Z-displacement of 1.9 mm, i.e. a real handling space of 86mm, in agreement with the simulation results. However, these performances tend to decrease during coupling due to some plane contacts or surface alignment. These preliminary results are encouraging, but further research is needed before the control system proposed below can be considered at this time.

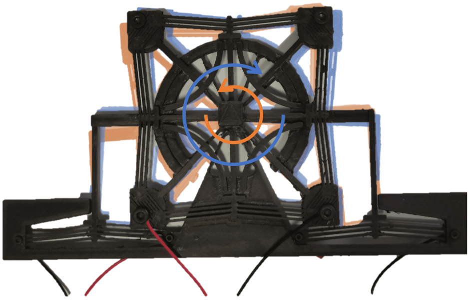

Fig. 21 Experimental validation of the rotational guiding system. The resulting displacements are displayed in transparency with respect to the manufactured configuration.

Table 3 Performance comparisons between the proposed XYZθ positioning system and previous reported parallel stages (*estimated)

References	Actuator	Dimension [mm]	Motion range [mm]
[31]	piezoelectric	105×105×105	1.5×1.5×1.5 [XYZ]
[32]		200×200×1	0.369×0.369, 1.28° [XYθ]
[33]	linear actuator	*250×250×(?)**	2.5×2.5, 10° [XYθ]
Proposed	electrothermic	206x109x21	3,8×3,8×2, 10.85° [XYZθ]

5 Control strategy of the actuator

The temperature rise takes much longer than the temperature-position conversion time, which induces a large dead-time τ, as shown in Fig. 22. The process is modelled by $\frac{ke^{-\tau s}}{1+Ts}$, identified from an open loop step response shown in Fig. 22. The Broïda method was chosen as the identification method because it is adapted to a stable system with a delay. It consists in observing the response and assimilating it to the response of a first order system (of time constant T), with a delay τ. The 28% and 40% ordinate points (giving respectively the times t_1 and t_2) allow to calculate T and τ by the formulas [34]:

$$\tau = 2.8t_1 - 1,8t_2 \tag{19}$$

$$T = 5,5(t_2 - t_1) \tag{20}$$

$$k = \frac{\Delta D}{\Delta V} \tag{21}$$

where k is the static gain of the system equal to the ratio between the output displacement and the input voltage.

The delay has already been observed in previous research using carbon-doped polymers [12]. By considering the time delay of some composites, it

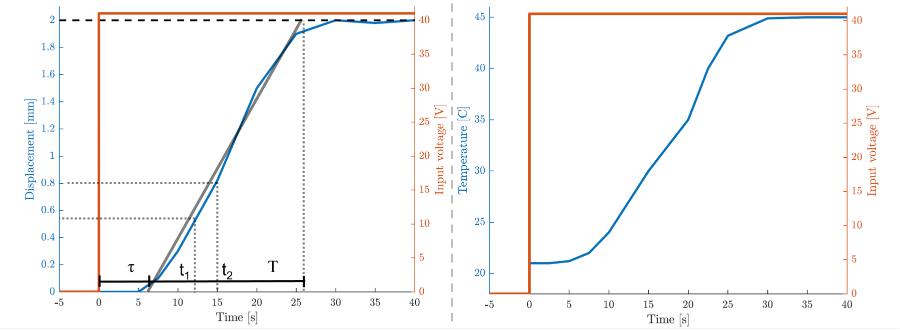

Fig. 22 On the left, the step response of the system representing the displacement of the actuator as a function of time following power-up. On the right, the intermediate response of the system where the temperature evolution after power up is represented. The delay is present during the temperature rise of the system.

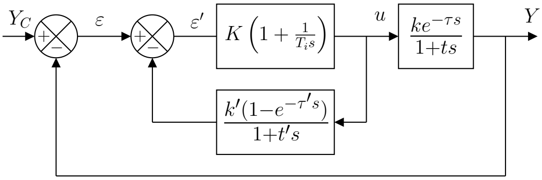

Fig. 23 Structure of Smith predictor based on PI control strategy

can be supposed that it is related to the quantity and quality of the carbon doping [35]. According to this hypothesis, which should be verified, a high carbon saturation could reduce or even cancel the delay as the behaviour of the composite would tend to approach that of a conducting material.

The use of a PID would be limited since the time delay would enter the loop and considerably decrease the performance of the control. A Smith predictor is a predictive controller designed to control systems with a significant feedback delay and here proposed with a PI controller. The PI controller is therefore set for a process without delay and then a final controller for the process with delay is calculated from the previous one, as shown in Fig. 23. After prior identification of the process, $\mathrm{k}' = \mathrm{k}$, $\tau' = \tau$ and $\mathrm{T}' = \mathrm{T}$ are set to have a process modelled as a first order system. According to [34], the PI controller was tuned such as $\mathrm{T_i} = \mathrm{T}$ and $\mathrm{K} = 0,7\frac{\mathrm{T}}{\tau\mathrm{k}}$.

The validation of this control strategy was done using the set-up illustrated in Fig. 24. A comparison of the experimental response before and after the use of the control loop is also shown in this figure. In view of the preliminary experimental results, this control strategy seems encouraging.

A displacement of 3.8mm is achieved with a bandwidth of 0.04Hz. This makes it a slow system but comparable to other actuators such as shape memory alloys, ionic electroactive polymers, or electroactive soft actuators [36–38]. Like most thermal systems, the behaviour of this actuator is dependent on its

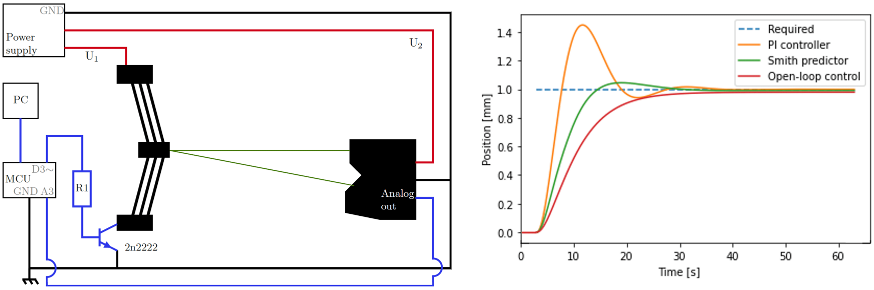

Fig. 24 Scheme of the experimental setup used to validate the actuator control strategy and step response with open-loop control, PI controller and Smith Predictor.

environment. The temperature and volume of surrounding air must be sufficient to ensure proper operation. In addition, depending on the speed of actuation, cooling systems may be required. To study the impact of the environmental temperature, the static error measured with respect to the setpoint is -0.028mm 3 minutes after the start of actuation. Therefore the system is stable under standard operating conditions.

6 CONCLUSIONS

In this paper, the feasibility of manufacturing a monolithic positioning system with built-in electrothermal actuators using 3D printers is presented. After introducing the design of the different components allowing to realize the displacements. The analysis and sizing of an electrothermal actuator was then carried out. The approach proposed here is based on the use of doping (actuation and heat dissipation) by design.

After validation of the models by finite element analysis, a prototype was built and evaluated. This prototype allows a positioning in a workspace of 86.2mm^3. This preliminary work has demonstrated the potential of using the 3D printer for the fabrication of monolithic systems integrating their actuators. However, there are still some aspects to be addressed, especially with regard to control. A control scheme for an actuator has been introduced in this paper, allowing to reduce the response time of the system. Further work will concern the extension of the proposed control strategy to the whole positioning system. Furthermore, although stable, this system remains slow, so it seems interesting to look at optimising the structure and other types of doping in order to address the dynamics of this system. Although the chosen filament has one of the lowest resistivities, it is still important and could be improved by doping it with another type of material, such as copper. The nature of the matrix determines the conduction and thermal expansion properties. Acrylonitrile Butadiene Styrene (ABS) and Polyethylene Terephthalate Glycol (PETG) have better characteristics than PLA and could offer better behaviour and a higher actuation frequency.

The non-linearities will have to be taken into account in order to extend the

proposed control strategy to the whole positioning system. Considering the electrical and material properties as constant over time allows the voltage to be controlled (constant resistance).
Although preliminary, this work has demonstrated the feasibility of producing actuators that can be manufactured by 3D printing in an integrated manner. This aspect is of interest for robotic applications where compactness and assembly are key issues [39]. A possible application of this positioning system would be to use it in low-cost atomic force microscopes for schools.

Acknowledgments This work was supported by the Investissements d'Avenir (Labex CAMI ANR-11-LABX-0004).

Declarations

Competing interests.
The authors declare that they have no competing interests that could have appeared to influence the work reported in this paper.
Authors' contributions.
Benjamin Calmé: Conceptualisation, Methodology, Investigation, Writing.
Lennart Rubbert: Methodology, Investigation, Review, Supervision.
Yassine Haddab: Methodology, Investigation, Review, Supervision.
Funding.
Not applicable
Availability of data and materials.
Not applicable

References

[1] Teo, T.J., Yang, G., Chen, I.-M.: Compliant Manipulators, pp. 1–64 (2014)

[2] Zhang, H., Wu, Z., Xu, Q.: Design of a New XY Flexure Micropositioning Stage With a Large Hollow Platform. Actuators **9**(3), 65 (2020). https://doi.org/10.3390/act9030065

[3] Hussein, H., Tahhan, A., Moal, P.L., Bourbon, G., Haddab, Y., Lutz, P.: Dynamic electro-thermo-mechanical modelling of a U-shaped electro-thermal actuator. Journal of Micromechanics and Microengineering **26**(2) (2016)

[4] Potekhina, A., Wang, C.: Review of Electrothermal Actuators and Applications, 28 (2019)

[5] Zhang, Z., Yu, Y., Liu, X., Zhang, X.: Dynamic modelling and analysis of V- and Z-shaped electrothermal microactuators. Microsystem Technologies **23**(8), 3775–3789 (2017)

[6] Moulton, T., Ananthasuresh, G.K.: Micromechanical Devices With Embedded Electro-Thermal-Compliant Actuation," Sens. Actuators A, 38–48 (2001)

[7] Alblalaihid, K., Overton, J., Lawes, S., Kinnell, P.: A 3D-printed polymer micro-gripper with self-defined electrical tracks and thermal actuator. Journal of Micromechanics and Microengineering **27**(4) (2017)

[8] Kim, H., Lee, S.: Characterization of Electrical Heating of Graphene/PLA Honeycomb Structure Composite Manufactured by CFDM 3D Printer. Fashion and Textiles **7**, 8 (2020)

[9] Ulkir, O.: Design and fabrication of an electrothermal MEMS micro-actuator with 3D printing technology. Materials Research Express **7**(7) (2020)

[10] Dijkshoorn, A., Werkman, P., Welleweerd, M., Wolterink, G., Eijking, B., Delamare, J., Sanders, R., Krijnen, G.J.M.: Embedded sensing: integrating sensors in 3-D printed structures. Journal of Sensors and Sensor Systems **7**(1), 169–181 (2018). https://doi.org/10.5194/jsss-7-169-2018. Accessed 2023-01-24

[11] Ryan, K.R., Down, M.P., Hurst, N.J., Keefe, E.M., Banks, C.E.: Additive manufacturing (3D printing) of electrically conductive polymers and polymer nanocomposites and their applications. eScience **2**(4), 365–381 (2022). https://doi.org/10.1016/j.esci.2022.07.003. Accessed 2023-01-24

[12] Zhuang, Y., Song, W., Ning, G., Sun, X., Sun, Z., Xu, G., Zhang, B., Chen, Y., Tao, S.: 3D–printing of materials with anisotropic heat distribution using conductive polylactic acid composites. Materials & Design **126**, 135–140 (2017)

[13] Dorigato, A., Moretti, V., Dul, S., Unterberger, S.H., Pegoretti, A.: Electrically conductive nanocomposites for fused deposition modelling. Synthetic Metals **226**, 7–14 (2017)

[14] Hussein, H., Le Moal, P., Bourbon, G., Haddab, Y., Lutz, P.: Modeling and Stress Analysis of a Pre-Shaped Curved Beam: Influence of High Modes of Buckling. International Journal of Applied Mechanics **07**(04) (2015)

[15] Henein, S., Spanoudakis, P., Droz, S., Myklebust, L., Onillon, E.: Flexure pivot for aerospace mechanisms. European Space Agency, (Special Publication) ESA SP (2003)

[16] Henein, S.: Flexures: simply subtle. Diamond Light Source Proceedings (2011)

[17] Henein, S.: Conception des structures articulées à guidages flexibles de haute précision. PhD thesis, EPFL (2000)

[18] Stranczl, M., Sarajlic, E., Gijs, M., Yamahata, C.: High-Angular-Range Electrostatic Rotary Stepper Micromotors Fabricated With SOI Technology. IEEE/ASME Journal of Microelectromechanical Systems **21**, 605–620 (2012)

[19] Hoang, K.T., Nguyen, D.T., Pham, P.H.: Impact of design parameters on working stability of the electrothermal V-shaped actuator. Microsystem Technologies (2019)

[20] Zhang, Z., Zhang, W., Wu, Q., Yu, Y., Liu, X., Zhang, X.: Closed-form modelling and design analysis of V- and Z-shaped electrothermal microactuators. J. Micromech. Microeng., 13 (2017)

[21] Ben Salem, M., Aiche, G., Haddab, Y., Rubbert, L., Renaud, P.: Additive Manufacturing of a Bistable Mechanism Using Fused Deposition Modeling: Experimental and Theoretical Characterization. In: Volume 5A: 43rd Mechanisms and Robotics Conference. American Society of Mechanical Engineers, Anaheim, California, USA (2019)

[22] El Magri, A., El Mabrouk, K., Vaudreuil, S., Touhami, M.: Mechanical properties of CF-reinforced PLA parts manufactured by fused deposition modeling. Journal of Thermoplastic Composite Materials **32** (2019). https://doi.org/10.1177/0892705719847244

[23] Fowler, R.M., Masseli, A., Pluimers, P., Magleby, S.P., Howell, L.L.: Flex-16: A large-displacement monolithic compliant rotational hinge. Mechanism and Machine Theory **82**, 203–217 (2014)

[24] Thalmann, E., Henein, S.: Triple Crossed Flexure Pivot Based on a Zero Parasitic Center Shift Kinematic Design. Journal of Mechanisms and Robotics **14**(4) (2022)

[25] Hricko, J., Havlik, S.: Compliant Mechanisms for Motion/Force Amplifiers for Robotics. In: Berns, K., Gorges, D. (eds.) Advances in Service and Industrial Robotics. Advances in Intelligent Systems and Computing, pp. 26–33. Springer, Cham (2020)

[26] Gao, X., Liu, Y., Zhang, S., Deng, J., Liu, J.: Development of a Novel Flexure-Based XY Platform Using Single Bending Hybrid Piezoelectric Actuator. IEEE/ASME Transactions on Mechatronics, 1–11 (2022). https://doi.org/10.1109/TMECH.2022.3150399

[27] Xu, Q.: Design and Development of a Compact Flexure-Based XY Precision Positioning System With Centimeter Range. IEEE Transactions

on Industrial Electronics **61**(2), 893–903 (2014). https://doi.org/10.1109/TIE.2013.2257139

[28] Zhu, J., Hao, G., Li, S., Yu, S., Kong, X.: A Mirror-Symmetrical XY Compliant Parallel Manipulator With Improved Performances Without Increasing the Footprint, (2021)

[29] Hao, G.: A 2-Legged XY Parallel Flexure Motion Stage with Minimised Parasitic Rotation. ARCHIVE Proceedings of the Institution of Mechanical Engineers Part C Journal of Mechanical Engineering Science 1989-1996 (vols 203-210) (2014)

[30] Calmé, B., Rubbert, L., Haddab, Y.: Towards a compact and low-cost mesoscopic XY positioning system using 3D printing of conductive polymers. In: 2022 International Conference on Manipulation, Automation and Robotics at Small Scales (MARSS) (2022). https://doi.org/10.1109/MARSS55884.2022.9870471

[31] Hao, G., Li, H.: Design of 3-legged XYZ compliant parallel manipulators with minimised parasitic rotations. Robotica **33**(4), 787–806 (2015)

[32] SP, B., Bharanidaran, R.: Design and testing of a compliant mechanism-based XYθ stage for micro/nanopositioning. Australian Journal of Mechanical Engineering **20**(4), 1185–1194 (2022)

[33] Lum, G.Z., Pham, M.T., Teo, T.J., Yang, G., Yeo, S.H., Sitti, M.: An XYθ flexure mechanism with optimal stiffness properties. In: 2017 IEEE International Conference on Advanced Intelligent Mechatronics (AIM), pp. 1103–1110 (2017). https://doi.org/10.1109/AIM.2017.8014166

[34] Bourgeois, J.-F.: Automatisme et régulation des équipements thermiques. Thermique pour l'industrie (1998). https://doi.org/10.51257/a-v1-be9590. Accessed 2023-01-30

[35] Bažant, Z.P.: Delayed thermal dilatations of cement paste and concrete due to mass transport. Nuclear Engineering and Design **14**(2), 308–318 (1970). https://doi.org/10.1016/0029-5493(70)90108-1. Accessed 2023-01-24

[36] Sheng, J., Desai, J.P.: A novel meso-scale SMA-actuated torsion actuator. In: 2015 IEEE/RSJ International Conference on Intelligent Robots and Systems (IROS), pp. 4718–4723 (2015). https://doi.org/10.1109/IROS.2015.7354049

[37] Song, S.-H., Lee, J.-Y., Rodrigue, H., Choi, I.-S., Kang, Y.J., Ahn, S.-H.: 35 Hz shape memory alloy actuator with bending-twisting mode. Scientific

Reports **6**(1), 21118 (2016). https://doi.org/10.1038/srep21118. Number: 1 Publisher: Nature Publishing Group. Accessed 2023-02-06

[38] Cao, S., Aimi, J., Yoshio, M.: Electroactive Soft Actuators Based on Columnar Ionic Liquid Crystal/Polymer Composite Membrane Electrolytes Forming 3D Continuous Ionic Channels. ACS Applied Materials & Interfaces **14**(38), 43701–43710 (2022). https://doi.org/10.1021/acsami.2c11029. Publisher: American Chemical Society. Accessed 2023-02-06

[39] Calmé, B., Rubbert, L., Haddab, Y.: Towards a Discrete Snake-Like Robot Based on SMA-Actuated Tristable Modules for Follow the Leader Control Strategy. IEEE Robotics and Automation Letters **8**(1), 384–391 (2023). https://doi.org/10.1109/LRA.2022.3224659. Conference Name: IEEE Robotics and Automation Letters